Scientific Reports

https://doi.org/10.1038/s41598-026-45267-w

Article in Press

mRNA profiling of mesenchymal stem cell-derived exosomes reveals their function in accelerating wound healing

Received: 17 November 2025

Accepted: 17 March 2026

Published online: 21 March 2026

Cite this article as: Than U.T.T., Nguyen H.T.T., Dang Q.M. *et al.* mRNA profiling of mesenchymal stem cell-derived exosomes reveals their function in accelerating wound healing. *Sci Rep* (2026). https://doi.org/10.1038/s41598-026-45267-w

Uyen Thi Trang Than, Hoai Thi Thanh Nguyen, Quang Minh Dang, Thu-Huyen Nguyen, Nhung Thi My Hoang, Thanh Hong Nguyen, Duc Minh Vu, Huong Thi Phi, Quynh Manh Luu, Xuan-Hai Do, Huy-Hoang Dao, Xuan-Hung Nguyen & Nam Hoang Nguyen

mRNA profiling of mesenchymal stem cell-derived exosomes reveals their function in accelerating wound healing

Uyen Thi Trang Than[1,2], Hoai Thi Thanh Nguyen[3], Quang Minh Dang[1], Thu-Huyen Nguyen[1], Nhung Thi My Hoang[3], Thanh Hong Nguyen[1,2], Duc Minh Vu[1,2], Huong Thi Phi[3], Quynh Manh Luu[3], Xuan-Hai Do[4], Huy-Hoang Dao[2], Xuan-Hung Nguyen[1,2], Nam Hoang Nguyen[3*].

Affiliation:

[1]Vinmec-VinUni Institute of Immunology, College of Health Sciences, VinUniversity, Hanoi 100000, Vietnam

[2]Vinmec Hi-Tech Center, Vinmec Healthcare System, Hanoi 100000, Vietnam

[3]VNU University of Science, Vietnam National University, Hanoi 100000, Vietnam

[4]Department of Practical and Experimental Surgery, Vietnam Military Medical University, 160 Phung Hung Street, Phuc La, Ha Dong, Hanoi, Vietnam

Corresponding to: Nam Hoang Nguyen, Email: namnh@hus.edu.vn, Phone: (+84) 913020286

ABSTRACT

Extracellular vesicles (EVs) are emerging as innovative tools for regenerative and therapeutic applications, including wound healing, owing to their ability to encapsulate bioactive agents from their parent cells. In this study, we profiled the transcriptome of umbilical cord mesenchymal stem cell (UCMSC)-derived exosomes (EXs) using RNA-seq and explored the functional roles of their transcriptome, particularly in cutaneous wound repair. We detected 4,578 protein-coding genes in UCMSC-derived EXs, of which 2,004 were upregulated, and 2,574 were downregulated relative to their secreting cells. Notably, many EX-enriched genes were associated with wound-healing biology, and pathway analysis revealed that upregulated exosomal genes were involved in GO terms and KEGG pathways related to DNA replication, ribosome function, cell cycle regulation, and pyrimidine metabolism. To validate UCMSC-EX's capability for wound healing predicted through *in silico* analyses, we further assessed EX penetration into the dermis, cellular uptake, and therapeutic efficacy in a burned mouse model. UCMSC-derived EXs efficiently penetrated human dermal tissue, were internalized by fibroblasts, and promoted fibroblast and keratinocyte proliferation and migration in 2D culture. *In vivo*, EX treatment accelerated wound closure, particularly during the early stages of healing. Overall, our findings demonstrate selective mRNA enrichment in UCMSC-derived EXs and highlight their promising therapeutic potential in cutaneous wound healing.

Keywords: Umbilical mesenchymal stem cell-derived exosomes, RNA-seq, exosome penetration, cutaneous wound healing.

Introduction

Exosomes (EXs) or small vesicles, a specific subtype of extracellular vesicles (EVs), are nanosized particles with diameters ranging from 30 to 150 nm [1]. They are secreted by virtually all cell types and could be obtained from conditioned media during cell culture *in vitro* and different biological fluids such as blood, urine, saliva, amniotic fluid, and breast milk [2,3]. The intravesicular contents of EVs display considerable diversity, which depends on their cellular origin, physiological state, and sorting mechanisms [4,5]; thus, EXs are packed with bioactive molecules, including proteins (tetraspanins, heat-shock proteins), nucleic acids (RNAs, microRNAs), and lipids (ceramides, cholesterol, sphingolipids) [4,6,7]. According to the latest update of ExoCarta, 13476 proteins, 3408 mRNAs, 10755 miRNAs, and 3946 lipid entries have been detected in exosomes (http://www.exocarta.org/, accessed 29/06/2025). Given the remarkable diversity in EX compositions linked to diverse cellular provenance, comprehensive omic-level profiling of these particles is of significant value. Such investigations hold the potential to unveil mechanisms and therapeutic targets worthy of further exploration and development.

In recent years, investigations have confirmed that mesenchymal stem cells (MSCs)-derived EXs possess a wide range of therapeutic capabilities across diverse conditions, including cardiovascular and renal protection, stroke, perinatal hypoxic-ischemic brain injury, hind-limb ischemia, immune-related diseases, cancer, wound healing, and even COVID-19 [8,9]. EXs derived from MSCs of varying origins or exposed to distinct external stimuli exhibit markedly different compositions of functional molecules and heterogeneous characteristics, consequently manifesting divergent therapeutic properties [9-11]. For example, bone marrow MSC-derived EXs have pronounced regeneration capacity through the induction of angiogenesis, adipose tissue MSC-derived exosomes show the most influential secretory activity and immunomodulation compared with MSCs derived from other sources, and umbilical cord mesenchymal stem cell (UCMSC)-derived EXs primarily participate in tissue repair [12]. Additionally, EXs have a significant impact on skin regeneration through modulating cell behaviors and functions of immune cells, fibroblasts, and endothelial cells, regulating inflammation and immune microenvironment, and promoting collagen deposition and angiogenesis by enabling intercellular crosstalk [13-16]. However, the mechanistic understanding of how EXs elicit their biological effects remains incomplete. While much of the focus has been on either EXs' broad interaction with cellular targets or protein-level characterisation of EXs' cargo, little emphasis has been placed on EXs' transcriptome.

Various groups have reported the presence of mRNA in EXs, as reviewed elsewhere [17]. However, the properties and functions of coding RNAs remain largely unexplored [18,19], which may strengthen the mechanistic understanding behind EXs' properties, such as wound healing. In this study, we investigated mRNA transcripts in UCMSC-derived EXs and simultaneously examined the wound healing capability of these EXs in both *in vitro* and *in vivo* models.

Results

Exosome characterization

We used differential centrifugation to isolate exosomes (EXs) from conditioned media of UCMSCs at P5. This population was examined for size distribution using the NTA technique and showed that the size distribution of EXs ranged from 40 nm to 350 nm, with the highest peak at 100 nm (Fig. 1a). Results from TEM imaging showed that a quite homologous cup-shaped morphology and smooth surface of EXs have been observed under TEM (Fig. 1b). Additionally, immunohistological analysis showed that exosomal markers of CD9, CD63, HSP70, and AGO2 have been detected in exosome fraction (Fig. 1c). The size of EXs analyzed using the NTA is consistent with the size observed under TEM, around 100 nm.

Protein-coding RNAs are differentially enriched in exosomes, and many are associated with wound-healing

In order to characterize the RNAs contained within EVs released from UCMSCs and secreting cells, an RNA sequencing approach was performed using the Nextseq 500/550 system (Illumina, USA). Statistics for alignment to the human HG38 genome and the proportion of uniquely mapped reads are shown in Table 1. More than 4 million uniquely mapped reads were obtained for all samples. The alignment rate was around 90% - 91% (Table 1).

Table 1. Read mapping, alignment, and feature-counting statistics

Category	Statistic	Exosome 1	Exosome 2	Exosome 3	UCMSC1	UCMSC2	UCMSC3
Sequence counts	Average number of uniquely mapped reads	4,173,608	5,111,878	4,518,578	5,167,534	8,615,614	8,097,777
	Average number of duplicated reads	5,250,685	7,443,151	4,478,099	5,610,149	11,512,273	12,144,406
Alignment	Total pair of reads	9,424,293	12,555,029	8,996,677	10,777,683	20,127,887	20,242,183
	Alignment rate	89.90%	89.85%	90.23%	90.25%	90.70%	91.38%
Mapping reads to	Total alignments	12,783,855	15,408,981	11,788,975	13,432,806	23,036,659	22,990,238

features	Successful assignment rate of reads to features	66.0%	74.4%	67.8%	70.8%	78.1%	81.2%

We first investigated the different biotypes of RNAs present in EXs. Results showed that the MGcound toolkit annotated relevant RNA features such as long RNA introns, long RNA exons, snoRNAs, and snaRNAs in the dataset (Fig. 2a-b). Regarding small non-coding RNAs, it was highlighted that SNORA49, RMRP-202, and SCARNA7 are downregulated in EXs, but RN7SL471P is upregulated in EXs. We observed a notable enrichment of various endogenous non-coding RNAs belonging to the RN7SL family, which encodes the signal recognition particle complex. Additionally, we found that our approach mainly captured protein-coding mRNAs in EXs (Fig. 2b).

To assess which coding transcripts were preferentially exported to EXs or retained in mother cells, using the R package DESeq2 [20], a differential analysis was performed to evaluate coding RNA abundances across UCMSCs and the EXs they secrete. Using a threshold of adjusted p-value = 0.05 and |Log2(Fold Change)| greater than 1, about 4578 genes were differentially expressed in UCMSC-derived EXs (Fig. 2c, Additional file 1 – Fig. 1). Among the 4,578 differentially expressed protein-coding genes, 2,004 (43.8%) were upregulated and 2,574 (56.2%) were downregulated in UCMSC-derived exosomes (padj < 0.05) (Fig. 2b-c). Genes in clusters identified through hierarchical clustering of top-upregulated genes in UCMSC-EXs could be found in the Additional file 2 – Table 1.

Notably, the most enriched transcripts in EXs included *Net 1* (Log_2FC = 7.03, padj = 1.50×10^{-31}), *Track2* (Log_2FC = 6.70, padj = 1.59×10^{-50}), *Rab13* (Log_2FC = 6.44, padj = 9.7×10^{-14}), and *Kif1c* (Log_2FC = 6.26, padj = 4.53×10^{-34}). Interestingly, *Anp32b* (Log_2FC = 5.38, padj = 2.69×10^{-21}), which harbors immune functions, and *Dgf11* (Log_2FC = 5.45, padj = 3.02×10^{-33}), which has multiple effects on cell development and physiology, were also one of the most enriched genes in EXs in our dataset. Interestingly, these genes are reported to be highly enriched in human umbilical cord vein endothelial cell-derived EXs. Therefore, our result strongly reproduced previous findings in EXs derived from endothelial cells [21], indicating perhaps the existence of conserved exosome mRNA markers.

In relation to wound healing, we found that many genes with the most significant magnitude of enrichment in EXs (evidenced by read counts and fold enrichment) are established potentiators of wound healing (Fig. 2b). These genes play diverse but relevant roles in the physiological wound-healing response. Of those, *Kif1c*, *Net1*, *Map4k4*, and *Coro1c* are applicable due to their involvement in regulating cellular migration during wound healing.

Other relevant genes included Discoidin domain receptor 2 (*Ddr2*), *Mmp2*, and zinc finger E-box binding homeobox 1 (*Zeb1*). The data of many

protein-coding mRNAs upregulated in EXs are associated with wound healing, indicating that UCMSC-derived EXs may play an essential role in the cutaneous healing process.

Network analysis and hierarchical clustering description indicated RNAs enriched in exosomes involved in the wound healing process

We performed a two-pronged approach to investigate the gene modules representing higher-level biological processes that are enriched within the community of coding RNAs in UCMSC-derived EXs. First, we constructed a protein interaction network for all genes contained within EXs and deconvolved network structures into clusters of highly interconnected nodes to define notable network structures that may underpin biological functions. In parallel, hierarchical clustering was performed to examine the pairwise correlations of genes strongly enriched in UCMSC-EXs. Pearson correlation coefficient was used to construct the distance matrix, with average as the agglomeration method. The goal was to identify clusters of highly correlated genes, suggesting a specific biological function enriched within EXs. The STRING protein interaction database was then used to map interactions between gene-encoded proteins contained within the cluster. Our rationale is that by combining two layers of evidence characterizing gene-gene association (by measuring the Pearson correlation coefficient), and protein interactions (by using the STRING database), we can comprehensively unveil emergent biological properties that may otherwise be missed.

For the first approach, after mapping exhaustive protein interactions between exosome-enriched genes, we used MCODE to deconvolve the network into significant clusters [22]. Two major networks were identified using a threshold score of 25 (Fig. 3a-b, Table 2, Supplemental Additional file 3 – Table 2).

Table 2. Network analysis statistics of clusters 1 and 2 - the two most significant clusters of protein interaction identified from exosome-enriched genes*.

	Cluster 1	Cluster 2
Number of nodes	200	55
Number of edges	9154	797
Network density	0.460	0.537
Network centralization	0.155	0.308

**Gene list contributed in clusters 1 and 2 could be found in Supplemental Additional file 3 – Table 2.*

Regarding the first network, the gene *Mcm3* is a central hub within this network, with connections to 200 nodes in the network (Fig. 3a). *Mcm3* promotes cellular proliferation and restricts apoptosis in many models and carcinoma cell types [23-25], and thus might be a central regulator of wound

healing. *Mcm3*'s ability to direct cell proliferation is related to its ability to regulate DNA replication. *Mcm3* is indispensable for initiating eukaryotic genome replication and is required to ensure that DNA replication is initiated precisely once per cell cycle. The second clusters include genes associated with mitochondria, many of which are subtypes of mitochondrial complex 1: NADH: ubiquinone oxidoreductase supernumerary subunits (*Nduf*) such as *Ndufs5*, *Ndufs8*, *Ndufb2*, *Ndufb6*, and *Ndufb10*. Many other members of this cluster are subunits of the mitochondrial ATP synthase (*Atp5j2*, *Atp5o*, *Atp5e*, *Atp5g1*, and *Atp5g3*) that have a role in driving the synthesis of ATP with the presence of a proton gradient, allowing cells to efficiently utilize the energy generated during electron transport [26]. Also, parts of this cluster are eight genes encoding mitochondrial and cellular ribosomal proteins that are part of the MRP and RPL protein families. Altogether, this cluster likely underlies major structural constituents of the mitochondrial ribosome and ATPase, which are essential for energy and protein regulation.

For the second approach, following hierarchical clustering, two significant clusters consisting of strongly correlated gene features were identified (Fig. 3c-d). To understand the biological processes governed by genes contained within these clusters, using the STRING protein interaction databases, we further identified the interconnected network motif (cluster) of protein interactions using MCODE. In cluster 1, genes in the MCODE-identified network are extensively documented to be involved in processes related to wound healing, notably cell migration and growth: *Ska3*, *Cenpu*, and *Cks1b*. Pathway analysis of clusters revealed the enrichment of GO processes related to organ development and inflammation, which are all key to wound healing (Additional file 4 – Fig. 2a). Regarding cluster 2, this network underpins mitotic cell division and cell cycle control, including *Cenpw*, *Brirc5*, *Cdca5*, and *Cenpm*. GO pathway enrichment analysis of this network has revealed that they contributed into intracellular protein transport and localization (Additional file 4 – Fig. 2b), which are critical for cellular functioning and division.

KEGG pathway enrichment and GO term analysis

KEGG pathway enrichment was employed to investigate the functional implication of genes enriched in EXs. Only protein-coding genes were considered. Data showed that genes upregulated in EXs were extensively involved in DNA replication (Fig. 4a). Other differentially enriched pathways included were related to cell cycle, splicesome, and pyrimidine metabolism (Additional file 5 – Fig. 3). Interestingly, regarding DNA replication, exosomal genes are components of many complexes required for DNA replication in eukaryotes. For example, among exosome-upregulated genes are five minichromosome maintenance (*Mcm*) genes that contributed significantly to the MCM complex, a DNA helicase functioning hydrogen bond between two DNA single strands. Additionally, exosomal genes encoding for protein epsilon 2, 3, and 4 are also crucial factors evolved in the DNA polymerase ε complex. Regarding the cell cycle pathway, which is essential to cell development, genes upregulated in EXs

contributed to all phases of the cell cycle, such as G1, S, G2, and M. These exosomal genes are primarily associated with assembling cyclin/CDKs to control phosphorylation of target genes (Additional file 4 – Fig. 2).

We were also interested in exosomal differential genes associated with the ECM-receptor interaction due to the ECM's extensive modulation of many mammalian biological processes relevant to skin wound healing. Notably, data indicated that numerous exosomally downregulated genes contributed to ECM interactions, namely those encoding for collagen, laminin, fibronectin, and tenascin (Fig. 4b). Other genes, including genes coding for Vitronectin, Thrombospondin, Arginin, and Perlecan, were also associated with ECM receptors herein. These genes directly activate various classes of cellular membrane receptors, such as Integrins, Proteoglycan, Glycoprotein, Ig-SF, and other combinations. Besides, some ECM genes, such as *Col2a*, *Col23*, and *Lamc3*, were still upregulated. Our data indicate that ECM genes are not selectively sorted into EXs; however, their expression in UCMSC-EX still reflects these particles' critical role in modulating ECM interactions.

We further extended our analysis to identify genes comprising the top GO terms. The top five enriched MF GO terms for differential genes are related to binding activities, such as cytoskeletal protein binding, microtubule binding, RNA binding, tubulin binding, and structural constituent of ribosome (Fig. 4c). Top five BP GO terms for differential genes are related to cellular proliferation, such as nuclear division, organelle fission, cell division, and mitotic cell cycle (Fig. 4d). We found over 200 genes contributing to the three most significant BP GO terms: cytoskeleton organization, mitotic cell cycle, and mitotic cell cycle process. These data reinforce that exosomal RNAs regulate cellular proliferation, relevant to injury healing.

UCMSC-EXs promote the wound-healing process *in vitro*

To address a part of the hypothesis generated from the bioinformatics analysis, we examined the capacity of EXs on the proliferation and migration of human dermal fibroblasts and keratinocytes, as well as mouse fibroblast NIH3T3, in 2D cultures. Results showed that UCMSC-EXs stimulated the proliferation of all three cell types compared to the control (Fig. 5a). Interestingly, the EXs induced the migration of two skin cell lines, NIH3T3 and HaCaT, but not the primary human dermal fibroblasts, compared to the control (Fig. 5**b-c**). These may be correlated to the data of protein-coding genes in EXs associated with the cell growth and cycle processes described in the section above.

UCMSC-EX penetration into the dermis and uptake by fibroblasts

Following the examination of EXs to enhance cell migration and proliferation, we further investigated the mechanism that EXs use to trigger cell behaviors using human skin models and fibroblasts in 2D cultures. Data showed that UCMSC-EXs injected into the epidermis could penetrate the dermis and disperse evenly in the dermis (Fig. 6a-b). Observation showed that EXs were also close to the nucleus, indicating the EXs internalized into the dermis cells (Fig.6c). Additionally, 2D cell

cultures revealed that EXs were uptaken by fibroblasts (Fig. 6d). These data indicate that UCMSC-EXs can internalize into cells and distribute to other layers of skin.

UCMSC-EXs promote the wound-healing process *in vivo*

We further tested the capacity of UCMSC-EXs in stimulating wound healing using burned skin mouse models. The healing process was followed up to 14 days. Results showed that the animal groups treated with EXs expressed a greater healing rate than the control and PBS-treated animals after being wounded until 10 days after treatment. However, the healing rate was similar for all treated groups from day 10. Interestingly, on the 14th, wounded areas associated with EX treatment healed faster than PBS treatment, but there was no difference among the other groups (Fig. 7a-b). These data indicate that EXs stimulate the healing process in the early period of the wound in this circumstance.

Discussion

Evidence has been increasing for the importance of mesenchymal stem cell-derived EXs for therapeutic purposes. Especially, EXs from UCMSCs have been shown to be involved in wound healing processes due to their potential to protect cells from oxidative stress-induced cell apoptosis *in vitro* [27] and promote cutaneous wound healing [28] and human skin rejuvenation [29]. Therefore, UCMSC-derived EXs are promising candidates for developing effective cutaneous wound-healing therapeutic products. Hence, in this study, we evaluated the mRNA profile in EXs released by primary human UCMSCs and the association of these molecules with wound healing processes *in vitro* and animal models. We first isolated UCMSC-derived EXs and demonstrated that these particles expressed typical cup-shaped morphology with a size between 40 - 150 nm and biomarkers of CD9, CD63, and AGO2. These were typical characteristics of EXs as described in previous reports [30,31].

Different molecules in EXs were reported to affect target cell functions. Focusing on skin wound healing and regeneration, several crucial growth factors essential for skin biology and healing have been reported previously [10,32-34]. Genetic materials, such as exosomal microRNAs, have also been reported to have a role in healing [35]. In this study, using RNA-seq as a proxy for transcriptome profiling, we discovered the identity of protein-encoding genes in EXs; more than 2000 genes are upregulated, indicating that these genes may be selectively sorted into EXs. Although pathway enrichment analysis indicated that exosomal mRNAs are associated with biological processes relevant to cell proliferation and migration, these findings do not establish a direct mechanistic link to wound repair. However, wound healing is a multicellular process involving inflammatory regulation, angiogenesis, and extracellular matrix remodeling, which were not mechanistically dissected in the present study [36]. Therefore, the observed association between exosomal transcript enrichment and wound-healing outcomes should be interpreted as

correlative and exploratory, providing a foundation for future mechanistic investigations rather than definitive evidence of causality.

Interestingly, we detect genes that are selectively enriched in exosomes, which are conserved across cell types and biological tissues. For instance, we found *Track2* to be one of the most enriched transcripts in EXs ($Log_2FC = 6.70$, padj = $1.59x10^{-50}$), which is similar to O'Grady et al. (2022), but the difference in the cell type of human umbilical vein endothelial cells [21]. Various mRNAs found to be enriched EXs reported by O'Grady were also reproduced in our dataset, notably *Rab13*, *Anp32b*, and ribosomal genes such as *Rpl14* and *Rpl26*. Of these genes, *Anp32b* was also one of the most enriched genes in EXs in our dataset ($Log_2FC = 5.38$, padj = $2.69x10^{-21}$); this gene modulates T lymphocyte phenotype and associated immunomodulatory pathways, leading to an autoreactive state [37]. Notably, many EX-enriched genes have functions relevant to wound healing. This function is relevant to wound healing, which requires fine-tuned control of inflammation as the initial step. Genes, including *Kif1c*, *Net1*, *Map4k4*, *Coro1c*, *Ddr2*, *Mmp2*, and *Zeb1,* enriched with the largest fold changes in UCMSC-derived EXs, could be potentiators of wound healing. *Kif1c* modulates directional cell migration - a process that is of vital importance to wound healing by stabilization of an extended and tense cell tail, facilitating persistent cell migration [38]. *Kif1c* is also involved in the turnover of podosome - actin-rich adhesions that enable cells to migrate [39]. Moreover, *Net1* knockdown reduced the wound-healing capacity of AGS gastric cancer cells by lowering their cell migration properties [40]. Similarly, *Map4k4* inhibition ameliorated the wound-healing and migratory properties of MDA-MB-231 breast cancer cells. *Coro1c* perturbation dampened persistent forward migration of mesenchymal cells in 1D and 3D cell culture systems by causing a loss in cell polarity [41]. Notably, the gene *Ddr2* is a tyrosine kinase receptor whose phosphorylation directly drives skin fibroblasts' capacity for proliferation, migratory capacity in response to chemotactic stimuli, and secretion of key factors involved in skin wound healing, such as *Mmp2* and fibrillar collagen [42]. In animal models, *Ddr2* ablation directly delayed the healing of skin injuries, in conjunction with the attenuated secretion of *Mmp2*, collagen type I, and crosslinking molecules that regulate the tensile strength of the skin [43]. The transcription factor *Zeb1* was also upregulated in EXs. It is a well-established potentiator of wound healing across diverse tissues, including the skin and cornea, by accelerating cellular proliferation, migration, and angiogenesis [39,44,45]. All of these genes enriched in UCMSC-derived EXs confirm the above hypothesis that UCMSC-derived EXs have roles in the wound healing process.

In this study, we did not observe the upregulation of ECM genes in exosomal components. The reason may be that the EXs were collected from basal conditions. If the MSCs were under stimulated conditions, such as the co-culture with the wounded fibroblast models, it could be induced by the signal molecules secreted from the target cells, as indicated in the impact of EV physiology on the characteristics of EV-producing cell transcriptomes [21].

To link the mRNA profile to the experimental cell behaviors, we examined the roles of UCMSC-derived EXs in cell proliferation and migration *in vitro* and in burned animal models. Similar to previous data, EXs could stimulate cell proliferation and migration in 2D cultures and heal the wound faster than the control group in burned mice [10,46]. The mechanism under this effectiveness may come from EXs internalized into cultured cells and penetrating into the skin and distributed around the area, as we have reported in Fig. 6. In both 2D cultures and skin *ex vivo* models, EXs were internalized into the cells and localized around the nucleus. This may indicate one mechanism of action by EXs to facilitate cell functions. This is important to the applicable approach regarding the real application of EXs, but it still requires deeper investigation. Furthermore, the efficacy of the healing rate may be due to the components equipped with EXs that induce regeneration at the wound site. UCMSC-derived exosomes are particularly effective during the early phase of healing (up to day 10), which aligns with the typical inflammatory and proliferative stages of tissue repair [47-49]. This observation suggests that exosomes may play a key role in modulating inflammation and promoting early tissue regeneration. However, the limited dosing duration (only for the first three days) used in this study might be a key factor in explaining why the effects were most prominent during the early healing stages [47]. This may indicate a prolonged treatment requirement depending on the wound's severity. It notes that despite the *in vivo* model being limited by a small sample size, this data provides preliminary data that directly link to the molecule-*in vitro*-*in vivo* peplines and evaluate trends and feasibility.

Human-derived EXs are frequently evaluated in murine models during the preclinical development of EX-based therapeutics. Despite interspecies differences, EX-mediated communication relies on mechanisms that are largely conserved across mammalian species. After internalization into target cells, EX cargo can modulate cellular signaling pathways, which are evolutionarily conserved between humans and mice [50,51]. If encapsulated human mRNAs are translated following uptake by murine cells, the resulting proteins would be of human origin. Many signaling and regulatory proteins involved in cellular communication and tissue repair are highly conserved between humans and mice [51]. Cross-species functionality has been widely observed in preclinical studies [50]. In this study, genes such as EIF5B, ADAMTS8, ZEB1, BCL11B, KIF1A, PTPN11, and CCNE2 (Additional file_Table 1) are known to share high amino-acid sequence identity between human and mouse [52]. This evolutionary conservation supports the likelihood that proteins translated from human exosomal mRNAs could retain functional activity within murine cellular pathways [53]. Numerous studies have demonstrated that human cell-derived EXs can be efficiently internalized by murine cells and exert biological effects in mouse models of tissue repair, inflammation, and regenerative medicine [8,54,55]. Therefore, murine models represent an established and informative system to investigate the biodistribution, safety, and functional effects of human EXs in vivo before clinical translation. Nevertheless, species-specific differences cannot be completely excluded. Additional studies evaluating protein expression or

functional activity of translated cargo in murine tissues would further strengthen the mechanistic understanding of these effects.

In conclusion, our study is the first reported mRNA profile in human UCMSC-derived EXs since the first report on exosomal mRNA profiles originated from mouse and human mast cell lines [5]. There have been several investigations on UCMSC-derived exosome miRNAs, but not yet on mRNAs. Although we identified selective enrichment of protein-coding mRNAs in UCMSC-derived exosomes and observed biological effects consistent with their predicted functions, the present study does not directly demonstrate translation of these exosomal mRNAs into functional proteins in recipient cells. Therefore, the contribution of transferred mRNAs to the observed regenerative effects remains inferential. Future studies employing approaches such as ribosome association assays, reporter-based translation tracking, nascent protein labeling, or quantitative proteomics following exosome uptake will be necessary to determine whether these transcripts are translated and functionally active in recipient cells. Additionally, this study being the pioneer study reported on the mRNAs packed into EXs and their effectiveness in promoting cell proliferation, migration, and wound closure, we have only investigated entire EXs in several wound healing processes. Further investigations are required for the association of exosomal genes with signaling pathways and their influence on other wound healing processes, such as angiogenesis, coagulation, scar formation, and the recovery level of skin structure.

Materials and methods

Ethical declarations

Ethical approval for the use of human MSCs from the umbilical cord and dermal fibroblasts was issued by the Vinmec International General Hospital Joint Stock Company's ethics committee (Ethical approval number: 02/2022/CN-HĐĐĐ VMEC). The umbilical cord tissues were collected from three healthy donors aged 20 to 40, and skin tissues for fibroblasts were collected from women who had undergone plastic surgery. All donors signed written informed consent before donating their samples, and experimental protocols were performed in accordance with the relevant guidelines and regulations and approved by the ethics committee.

For the use of animals and all experimental protocols involving animals, the study was approved by the Institutional Review Board at Dinh Tien Hoang Institute of Medicine. The Ethical approval number IRB-A 2203. We confirmed that all experiments and methods used in this study were performed in accordance with relevant regulations and the ARRIVE (Animal Research: Reporting of In Vivo Experiments) guideline.

EX preparation

The primary UCMSCs from three independent donors at passage 3 (P3) were supplied by the EV group (Vinmec Hi-Tech Center) and expanded to

P5 in DMEM/F12 (Gibco, Massachusetts, USA) supplemented with 10 % FBS (Gibco, Massachusetts, USA) (v/v) at 5 % CO_2 and 37 ^oC. The protocol of UCMSC isolation was described previously by Le et al. [56]. All UCMSCs meet the ISCT requirements, including fibroblast-like morphology, > 95% positive markers (CD73, CD90, CD105), < 2% negative markers (CD45, CD34, CD11b, CD19, and HLA-DR), and capacity for trilineage differentiation and colony-forming units [56]. UCMSCs P5 were seeded with a density of 5000 cells/cm^2 in a T75 flask with EV-depleted culture media (90 % DMEM/F12 and 10 % EV-depleted FBS). To prepare EV-depleted FBS, FBS was centrifuged at 120,000 × g / 18 hours /4 °C. After four or five days of incubation, when cells reached 80 % confluency, the conditioned medium was collected and centrifuged at 300 × g / 10 minutes / 4 °C to remove cell debris. Then, apoptotic bodies and microvesicles (MV) were removed using sequential centrifugations at 2,000 × g / 20 min / 4 °C and 16,500 × g / 30 min / 4 °C, respectively. The remaining supernatant was collected and centrifuged at 100,000 × g / 90 min / 4 °C for EXs (Optima XPN-100 Ultracentrifuge, Beckman Coulter, California, USA) [10]. All EXs were resuspended in PBS and stored at −80 °C for further use.

Western blot

Three EXs samples from three UCMSCs (named EX1, EX2, and EX3, respectively) were mixed with RIPA buffer (Thermo Scientific, USA) in an equivalent volume, incubated for 30 min at 4 °C, and then centrifuged at 16,000 x g for 20 min at 4 ^oC for protein extraction. Protein concentration was determined using the Pierce™ BCA Protein Assay Kit (Thermo Scientific, USA) and the optical densitometry method (Optical density - OD) at 560nm. A total 10 - 20 µg exosome proteins was loaded into each well and separated using a 4-12 % NuPAGE gel (Invitrogen, USA) at 200 V for 60 min at 4 °C prior to being transferred to a PVDF membrane (AmershamTM, GE Healthcare Life Science, Illinois, US) at 200 mA for 2 hours at 4 °C. After that, membranes were incubated with primary antibodies diluted in TBST solution for anti-CD63 (dilution 1:200), anti-CD9 (dilution 1:100), anti-HSP70 (dilution 1:200), and anti-AGO2 (dilution 1:100) (Abcam, Cambridge, UK) overnight at 4°C. The primary antibodies were washed before incubating with secondary antibody Mouse IgG (Amersham ECL Mouse IgG, HRP-linked whole Ab, GE Healthcare Life Sciences, Pittsburgh, USA). Antibody binding was detected by ECL chemiluminescent substrate (Sigma-Aldrich, Singapore) and imaged on an ImageQuant LAS 500 (GE Healthcare Life Science, Illinois, US) [57].

Transmission electron microscopy (TEM)

EXs were fixed with 4% paraformaldehyde and subsequently placed onto a carbon grid (Ted Pella Inc., California, USA). Samples were then washed before being stained and dried at room temperature. Finally, samples were examined and photographed by a Transmission Electron Microscopy JEOL 1100 (TEM, JEOL Ltd., Tokyo, Japan) at 80 kV at the National Institute of Hygiene and Epidemiology (NIHE) [57].

Exosome label, uptake, and penetration

EXs were stained using the ExoGlow-Membrane EV Labeling Kit (System Biosciences, USA) according to the manufacturer's protocol. In brief, the labeling buffer and dye were mixed with 100 µg of EXs and incubated for 30 minutes at room temperature in the dark. The reaction mixture was then applied to a PD SpinTrap G-25 column (Cytiva Sweden, UK) to eliminate unbound dye and centrifuged at 800 × g for 2 minutes. The labeled EXs were collected in the first eluate [58].

EX uptake assays were conducted using human dermal fibroblasts provided by the EV group (Vinmec HiTech Center). Cells were seeded into a 96-well plate and incubated with labeled EXs. After four hours of incubation at 37°C, the medium containing excess labeled EXs was removed, and the cells were washed with PBS. Then, cells were fixed with PFA 4 % for 20 minutes, followed by nuclear staining with DAPI (4′,6-diamidino-2-phenylindole) (Thermo Fisher Scientific). EX uptake was evaluated by using confocal microscopy [58].

EX penetration examinations were tested on *ex vivo* human skin models. The skin was cut into approximately 1 x 1 cm in length and placed on clean dishes. 100 µL of fluorescence-labeled EX solution (50 µg of exosomal protein) was injected into the epidermis (five injection sites) using a 1 mL syringe equipped with a 32G needle. Skin explants injected with fluorescence-labeled EXs were cultured for 12 hours before being fixed and stained to investigate the penetration of EXs into the dermis [59].

RNA library preparation and transcription sequencing

Total RNAs from EXs and secreting UCMSCs (three individual biological samples) were extracted using Trizol™ method. Extracted RNA was quantified using Qubit RNA HS Assay Kit (Thermo Fisher, USA) to measure total RNA concentration. The optimal range for purified RNA is from 5 ng/µL to 10 ng/µL in RNase/DNase-free water. RNA integrity (RIN) was measured by the Agilent 4200 TapeStation system using High Sensi RNA ScreenTape (Agilent, USA). An amount of 50 ng total RNA was used for reverse transcription using random hexamer primers to synthesize the first cDNA strand. The second cDNA strand was synthesized by DNA polymerase using the first cDNA strand as a template. The cDNA fragments were then end-repaired and A-tailed to generate the 5' overhangs for indexing adapter ligation. The A-tailed cDNA fragments were ligated with an indexing adapter, followed by amplification with i5 and i7 indexing primers for sample multiplexing. The indexed libraries were pooled and hybridized with the Illumina exome sequencing panel (Illumina, USA). Targeted regions of interest were then captured using Streptavidin Magnetic Beads, followed by the final amplification step to achieve an enriched library. The quality of the enriched library was then assessed on Agilent 4200 TapeStation (Agilent, USA) using High-Sensitivity D1000 Tapes. The library concentration was measured by Qubit 4.0 Fluorimeter using Qubit dsDNA BR Assay Kit (Thermo Fisher, USA). The library was diluted to 4 nM using the resuspension buffer (RSB), followed by a denaturing step in the presence of NaOH 0.2 N by ratio 1:1 (v/v). The denatured library was diluted with denaturing buffer HT1 to achieve a 20 pM denatured library solution. The denatured library

was then diluted to the final concentration of 1.3 pM in a total volume of 1.3 mL for sequencing. Sequencing was done on the Nextseq 500/550 system using Nextseq High Output v2.5 (300 cycles) (Illumina, USA).

RNA-seq data analysis

At least 9 million paired-end reads (2 x 75 base pairs or bp) were obtained for each replicate. Raw quality sequencing was assessed using FastQC v0.11.9 [60] both before and after adapter trimming, and all samples passed scores on all FastQC criteria. Nextera adapter sequences, low-quality base calls (Phred score < 15), and short reads (read length < 20 base pairs) were trimmed using Trim Galore v0.6.2 [61]. FASTQ paired-end reads were aligned using HISAT2 v2.2.1 [62] to the human GRCh38 genome build from Ensembl [63]. The resulting BAM files were sorted by read name and chromosome position with Samtools v1.8 [64]. Transcripts were quantified via the FeatureCounts function of the Bioconductor R package Rsubread v1.6.4 [65], counting non-strand-specific fragments instead of reads. MultiQC (v1.9) [66] was used to aggregate FastQC, HISAT2, and FeatureCounts results.

RNA biotype classification and analysis

To quantify the presence of different RNA biotypes, including long RNAs (both coding and non-coding) and short RNAs, the MGcount toolkit (v1.1.0) [67]was used using parameters suitable for unstranded paired-end reads. MGcount hierarchically assigns RNA-seq reads present to genomic annotated features in three pre-defined sequential rounds based on transcript body length: small RNA, long RNA exon, and long RNA introns, then quantifies these RNA features. An integrated GRCh38 .gtf file was used in this analysis to annotate relevant RNA features such as long RNA introns, long RNA exons, snoRNAs, and snaRNAs in the dataset if they are present. The RNA feature expression matrix from MGcount was used as input to DESeq2 for differential analysis of RNA biotype abundance between exosomes and cells, enabling the identification of features enriched in exosomes. RNA biotype distribution and differential abundance were visualized using a series of R packages, including Enhanced Volcano and ggplot2.

Differential analysis

Differential analysis was performed on the count matrix using R version 4.2 and the R package DESeq2 v3.15 to compare exosomes and cells from which they are excreted [20]. Data was normalized using DESeq2's built-in median-of-ratios method to account for library depth and RNA composition across samples. Genes with low counts (the sum of counts is less than 60 across all samples) were filtered, as they mostly reflect noise in the dataset.. Heatmaps were generated with the R package pheatmap (v1.0.12, available at: https://github.com/raivokolde/pheatmap). P values were adjusted using the FDR method for multiple testing. Significantly differentially expressed genes (DEGs) were selected with an FDR < 0.05 and $\log_2$ fold change ≥ 1 or <-1 for comparison between exosomes and cells. Volcano plots were built using the R package Enhanced Volcano (v1.16.0) [68].

Pairwise correlations and hierarchical clustering

The top significant DEGs in upregulated and downregulated gene sets were filtered according to adjusted p values (adjusted $p < 0.05$) and $\log_2$Fold Change ($|log2FC| > 2$). Using the average agglomeration method, the distance matrix was constructed using the Pearson correlation coefficient of the logarithm of the normalized expression of DEGs in all samples. The gene-gene correlation heatmap was visualized using the heatmap.2 function of the R package gplots (version 3.1.3) [69].

Pathway enrichment analysis

Significant DEGs (adjusted p-value < 0.05 and |Log2FC| > 1) were used to identify over-represented Gene Ontology (GO) terms (GO Biological Process and Molecular Function databases) and enriched pathways annotated in the Kyoto Encyclopedia of genes and genomes (KEGG) database. Enriched pathways with $p < 0.05$ were considered statistically significant. Analysis and visualization of GO term overrepresentation were performed using the R package ClusterProfiler v4.4.4 [70]. KEGG pathway enrichment and visualization were performed via the R package gage (v2.52.0) [71] and KEGG v1.42.0 [72].

Network analysis

Protein-protein interactions of the genes enriched in exosomes or part of the exosome-enriched cluster were constructed using the STRING protein database (https://string-db.org/). Upregulated genes were filtered based on the following thresholds: adjusted p-value < 0.05 and Log2FC > 1. Protein interactions with a confidence score of more than 0.4 were chosen, indicating moderate to strong evidence of protein interaction. The largest subnetwork was selected for further analysis to filter proteins or protein pairs with few interactions with other nodes in the network. Using default parameters, the Cytoscape plug-in Molecular Complex Detection (version 1.32) [22] was used to identify prominent subnetworks and clusters within the protein interaction network. Network clusters with an MCODE score greater than 25 were chosen to analyze upregulated genes.

Proliferation Assay

Human dermal fibroblasts were seeded at 2,500 cells/well of a 96-well plate and incubated in DMEM/F12 supplemented with 10% EV-depleted FBS and 10 µg EXs at 37 °C and 5 % CO_2 for 48 hours to proliferate. The control group consisted of cells incubated with DMEM/F12 supplemented with 10 % EV-depleted FBS. The cell proliferation rate was assessed by performing a 3-(4,5-dimethylthiazol-2-yl)-2,5-diphenyl tetrazolium bromide (MTT) assay (Abcam, Cambridge, UK) following the manufacturer's protocols. The proliferation rate was equivalent to the relative absorbance measured at 562 nm (SpectraMax M3, Molecular Devices, California, USA) at time points of 0 hours (as used for normalization) and 48 hours, with a higher OD value indicating a higher proliferation rate.

Migration Assay

Human dermal fibroblasts were seeded at 1.05×10^5 cells/ well of a 24-well plate at 37 °C and 5 % CO_2 for attachment. After reaching 100% confluency, fibroblasts were incubated with Mitomycin C (10 µg/mL) for 2 hours to inhibit cell proliferation. A physical scratch was created on the cell attachment layer, and detached cells were removed by washing with media. The cells were then treated with DMEM/F12 supplemented with 10% EV-depleted FBS and 10 µg EXs, and the control cells were treated with DMEM/F12 supplemented with 10 % EV-depleted FBS. Cell migration to close the wound area was captured by an inverted microscope at multiple time points. The wound area was measured using ImageJ software (version 1.48) and calculated for the closure percentage over time, representing the cell migration rate.

Wound healing animal model

Swiss male mice (50 - 60 g, 8 - 10 weeks old) were supplied by the Center of Experimental Animals - Vietnam Military Medical University. Mice were supplied with food and water daily in a 12-hour light/dark cycle condition. The mice were anesthetized with intraperitoneal ketamine (50 mg/mL), a 140 mg/kg body weight dosage. The dorsum of mice was shaved using an electric shaver, and the skin was disinfected with an alcohol swab. A metal plate (1.5 × 1.5 × 0.3 cm) was sterilized with 70 % ethanol and then heated to reach 250^{o}C before being placed immediately on the skin for 10 seconds to create burned wounds. A wound would be made on the right side of the dorsum. For anesthesia and pain relief, animals were injected intraperitoneally with Ketamine/Xylazine at a ratio of 100/10/kg body weight (diluted with phosphate-buffered saline (PBS) solution) before skin burn model induction. After wound induction, animals were kept warm, individually, and the cages were lined with soft cotton. Post-operative analgesia was managed during the first 3 days using buprenorphine (Norspan, LTS Lohmann Therapie-Systeme AG, Germany). The drug was diluted in PBS and administered via subcutaneous injection at a dosage of 0.1 mg/kg every 8-12 hours. The mice were randomly divided into three groups (n = 3 each), including group 1: non-treated, group 2: injected intradermally with 100 µL PBS, and group 3: injected intradermally with 100 µL EX solution (1 µg/1 µL). Wounded animals were immediately treated with substances as designed after creating the wounds, PBS, and exosome (from EX1 sample) injections for the first three days, and all were followed up for 14 days. Wounds were observed every day. Quantitative analysis of wound closure was performed using ImageJ software (NIH, USA). To ensure accuracy, the pixel-to-length ratio was calibrated using a metric ruler included in the photographic field. Wound surface area was measured by manually tracing the wound perimeter and imaged at day 6, day 10, and day 14. % wounded closure = [(area day 0 – area day T)/area day 0] x 100 %.

Mice were humanely euthanized at the end of the experiment at the Animal Center of the Military Medical Academy by the Center's technicians. The animals were euthanized using CO_2 in a specialized glass chamber. Each mouse was placed into the chamber, which was then filled with 100 % compressed CO_2 at a flow rate of 30 - 70% of the chamber

volume per minute to ensure rapid loss of consciousness and to minimize pain or distress. Each mouse was observed individually to detect cessation of breathing and corneal opacity (gradual clouding or paling of the eyes), which typically occurs after 2–3 minutes of gas exposure. CO_2 flow was maintained for at least one additional minute after respiratory arrest was confirmed.

Statistical analysis

N represents the number of independent replicates per group, as detailed in each figure legend. The false discovery rate (FDR) was calculated for each statistical test to correct for errors of multiple testing. The Benjamini and Hochberg (BH) method was used to compute the false discovery rate (FDR) for each statistical test. The thresholds for DEG detection were specified in the Methods section. Statistical testing was performed using built-in packages in R (version 4.2) (R Core Team, 2022) and Python (version 3.10).

Data from the wet lab were presented in Mean ±SD. The student's t-test and ANOVA were used for comparisons between groups. The p-value<0.05 was used to determine the significant difference.

Abbreviations

EVs	Extracellular vesicles
EXs	Exosomes
MSCs	Mesenchymal stem cells
UCMSCs	Umbilical cord-derived mesenchymal stem cells
GO	Gene Ontology
KEGG	Kyoto encyclopedia of genes and genomes
DEGs	Differentially expressed genes
GAGE	Generally Applicable Gene-set Enrichment
DMEM/F12	Dulbecco's Modified Eagle medium/Ham's F-12
FBS	Fetal bovine serum
MVs	Microvesicles
PBS	Phosphate buffer saline
BCA	Bicinchoninic acid
PVDF	Polyvinylidene fluoride
TBST	Tris-buffered saline with Tween® 20
NTA	Nanoparticle tracking analysis
TEM	Transmission electron microscopy
FDR	False discovery rate
BH	Benjamini and Hochbergw

Supplementary Information

Additional file 1 – Fig. 1
Additional file 2 – Table 1
Additional file 3 – Table 2
Additional file 4 – Fig. 2
Additional file 5 – Fig. 3

Acknowledgment

We sincerely thank Dr. Nguyen Thi Nhan for their valuable bioinformatics analysis and review advice.

Funding

This project was funded by the VinIF project code VINIF.2021.DA00193.

Data availability

All data generated in this study are provided in the articles and available in online supplementary files. All RNA sequencing data reported in this publication have been deposited in NCBI's Gene Expression Omnibus and are accessible through the GEO accession number: GSE252017.

Declarations

Ethics approval and consent to participate

Ethical approval for the use of human MSCs from the umbilical cord and dermal fibroblasts was issued by the Vinmec International General Hospital Joint Stock Company's ethics committee (Ethical approval number: 02/2022/CN-HĐĐĐ VMEC). The umbilical cord tissues were collected from three healthy donors aged 20 to 40, and all donors signed the written informed consent before the samples were collected.

The use of animals in this present study followed guidelines for animal treatment and complied with the relevant legislation from the Institutional Review Board at Dinh Tien Hoang Institute of Medicine (Ethical approval number: IRB-A 2203).

Consent for publication

Not applicable.

Competing interests

The authors declare that they have no competing interests.

References

1. Liangsupree, T., Multia, E. & Riekkola, M.-L. Modern isolation and separation techniques for extracellular vesicles. *Journal of Chromatography A* **1636**, 461773 (2021).
2. Zhang, H. et al. Exosome-induced regulation in inflammatory bowel disease. *Frontiers in Immunology* **10**(2019).
3. Boriachek, K. et al. Biological functions and current advances in isolation and detection strategies for exosome nanovesicles. *Small* **14**, 1702153 (2018).
4. Cañas, J.A., Sastre, B., Rodrigo-Muñoz, J.M. & del Pozo, V. Exosomes: A new approach to asthma pathology. *Clinica Chimica Acta* **495**, 139-147 (2019).
5. Valadi, H. et al. Exosome-mediated transfer of mRNAs and microRNAs is a novel mechanism of genetic exchange between cells. *Nature cell biology* **9**, 654-659 (2007).
6. Rahmati, S., Shojaei, F., Shojaeian, A., Rezakhani, L. & Dehkordi, M.B. An overview of current knowledge in biological functions and potential theragnostic applications of exosomes. *Chemistry and physics of lipids* **226**, 104836 (2020).
7. Dai, J. et al. Exosomes: key players in cancer and potential therapeutic strategy. **5**, 145 (2020).
8. Phinney, D.G. & Pittenger, M.F. Concise review: MSC-derived exosomes for cell-free therapy. *Stem Cells* **35**, 851-858 (2017).

9. Lee, B.-C., Kang, I. & Yu, K.-R. Therapeutic features and updated clinical trials of mesenchymal stem cell (MSC)-derived exosomes. *Journal of Clinical Medicine* **10**, 711 (2021).
10. Hoang, D.H. et al. Differential wound healing capacity of mesenchymal stem cell-derived exosomes originated from bone marrow, adipose tissue and umbilical cord under serum- and xeno-free condition. *Front Mol Biosci* **7**, 119 (2020).
11. Mendt, M., Rezvani, K. & Shpall, E. Mesenchymal stem cell-derived exosomes for clinical use. *Bone Marrow Transplantation* **54**, 789-792 (2019).
12. Wang, Z.-g. et al. Comprehensive proteomic analysis of exosomes derived from human bone marrow, adipose tissue, and umbilical cord mesenchymal stem cells. *Stem Cell Research & Therapy* **11**, 511 (2020).
13. Joorabloo, A. & Liu, T. Engineering exosome-based biomimetic nanovehicles for wound healing. *Journal of Controlled Release* **356**, 463-480 (2023).
14. Han, X. et al. Exosomes derived from autologous dermal fibroblasts promote diabetic cutaneous wound healing through the Akt/β-catenin pathway. *Cell Cycle* **20**, 616-629 (2021).
15. Dalirfardouei, R., Jamialahmadi, K., Jafarian, A.H. & Mahdipour, E. Promising effects of exosomes isolated from menstrual blood-derived mesenchymal stem cell on wound-healing process in diabetic mouse model. *Journal of Tissue Engineering and Regenerative Medicine* **13**, 555-568 (2019).
16. Belvedere, R. et al. Mesoglycan induces the secretion of microvesicles by keratinocytes able to activate human fibroblasts and endothelial cells: A novel mechanism in skin wound healing. *European Journal of Pharmacology* **869**, 172894 (2020).
17. Iqbal, Z. et al. Exosome for mRNA delivery: strategies and therapeutic applications. *Journal of Nanobiotechnology* **22**, 395 (2024).
18. Ma, H., Zhang, S., Xu, Y., Zhang, R. & Zhang, X. Analysis of differentially expressed microRNA of TNF-α-stimulated mesenchymal stem cells and exosomes from their culture supernatant. *Archives of Medical Science* **14**, 1102-1111 (2018).
19. Yang, B.-c. et al. Human umbilical cord mesenchymal stem cell-derived exosomes act via the miR-1263/Mob1/Hippo signaling pathway to prevent apoptosis in disuse osteoporosis. *Biochemical and Biophysical Research Communications* **524**, 883-889 (2020).
20. Love, M.I., Huber, W. & Anders, S. Moderated estimation of fold change and dispersion for RNA-seq data with DESeq2. *Genome Biology* **15**, 550 (2014).
21. O'Grady, T. et al. Sorting and packaging of RNA into extracellular vesicles shape intracellular transcript levels. *BMC Biol* **20**, 72 (2022).
22. Bader, G.D. & Hogue, C.W.V. An automated method for finding molecular complexes in large protein interaction networks. *BMC Bioinformatics* **4**, 2 (2003).
23. Li, H.T. et al. Diagnostic and prognostic value of MCM3 and its interacting proteins in hepatocellular carcinoma. *Oncol Lett* **20**, 308 (2020).
24. Valverde, L.d.F. et al. MCM3: a novel proliferation marker in oral squamous cell carcinoma. *Applied Immunohistochemistry & Molecular Morphology* **26**, 120-125 (2018).
25. Gao, Z. et al. PLK1 promotes proliferation and suppresses apoptosis of renal cell carcinoma cells by phosphorylating MCM3. *Cancer Gene Therapy* **27**, 412-423 (2020).
26. Human Gene ATP5F1C (ENST00000356708.12) from GENCODE V47.
27. Zhang, B. et al. Exosomes from human umbilical cord mesenchymal stem cells: identification, purification, and biological characteristics. **2016**, 1929536 (2016).
28. Zhang, B. et al. HucMSC-exosome mediated-Wnt4 signaling is required for cutaneous wound healing. *Stem Cells* **33**, 2158-68 (2015).
29. Kim, Y.J. et al. Exosomes derived from human umbilical cord blood mesenchymal stem cells stimulates rejuvenation of human skin. *Biochem Biophys Res Commun* **493**, 1102-1108 (2017).
30. Nikfarjam, S., Rezaie, J., Zolbanin, N.M. & Jafari, R. Mesenchymal stem cell derived-exosomes: a modern approach in translational medicine. *Journal of Translational Medicine* **18**, 449 (2020).

31. Shabbir, A., Coz, A., Rodriguez, L., Salgado, M. & Badiavas, E. Mesenchymal stem cell exosomes induce the proliferation and migration of normal and chronic wound fibroblasts, and enhance angiogenesis in vitro. *Stem Cells and Development*, 150413083553001 (2015).
32. Than, U.T.T., Guanzon, D., Leavesley, D. & Parker, T. Association of extracellular membrane vesicles with cutaneous wound healing. *Int J Mol Sci* **18**(2017).
33. Zhu, B. et al. Stem cell-derived exosomes prevent aging-induced cardiac dysfunction through a novel exosome/lncRNA MALAT1/NF-kappaB/TNF-alpha signaling pathway. *Oxid Med Cell Longev* **2019**, 9739258 (2019).
34. Hong, P., Yang, H., Wu, Y., Li, K. & Tang, Z. The functions and clinical application potential of exosomes derived from adipose mesenchymal stem cells: a comprehensive review. *Stem Cell Res Ther* **10**, 242 (2019).
35. Than, U.T.T., Guanzon, D., Broadbent, J.A., Parker, T.J. & Leavesley, D.I. Deep sequencing microRNAs from extracellular membrane vesicles revealed the association of the vesicle cargo with cellular origin. *International Journal of Molecular Sciences* **21**, 1141 (2020).
36. Sonnemann, K.J. & Bement, W.M. Wound repair: toward understanding and integration of single-cell and multicellular wound responses. *Annu Rev Cell Dev Biol* **27**, 237-63 (2011).
37. Chemnitz, J. et al. The acidic protein rich in leucines Anp32b is an immunomodulator of inflammation in mice. in *Scientific Reports* Vol. 9 4853 (2019).
38. Theisen, U., Straube, E. & Straube, A. Directional persistence of migrating cells requires Kif1C-mediated stabilization of trailing adhesions. *Developmental Cell* **23**, 1153-1166 (2012).
39. Kopp, P. et al. The kinesin KIF1C and microtubule plus ends regulate podosome dynamics in macrophages. *Mol Biol Cell* **17**, 2811-23 (2006).
40. Murray, D., Horgan, G., Macmathuna, P. & Doran, P. NET1-mediated RhoA activation facilitates lysophosphatidic acid-induced cell migration and invasion in gastric cancer. *Br J Cancer* **99**, 1322-9 (2008).
41. Williamson, R.C. et al. Coronin-1C and RCC2 guide mesenchymal migration by trafficking Rac1 and controlling GEF exposure. *J Cell Sci* **127**, 4292-307 (2014).
42. Olaso, E. et al. Discoidin domain receptor 2 regulates fibroblast proliferation and migration through the extracellular matrix in association with transcriptional activation of matrix metalloproteinase-2. *The Journal of Biological Chemistry* **277**, 3606-3613 (2002).
43. Olaso, E., Lin, H.C., Wang, L.H. & Friedman, S.L. Impaired dermal wound healing in discoidin domain receptor 2-deficient mice associated with defective extracellular matrix remodeling. *Fibrogenesis Tissue Repair* **4**, 5 (2011).
44. Lan, H. et al. Pro-angiogenic role of ZEB1 in skin wound healing by upregulating VEGFA via microRNA-206 suppression. *Experimental Dermatology* **31**, 1392-1401 (2022).
45. Zhang, X., Wang, M., Zhang, Y., Yang, J. & Duan, W. Knockdown of CENPU inhibits cervical cancer cell migration and stemness through the FOXM1/Wnt/β-catenin pathway. *Tissue and Cell* **81**, 102009 (2023).
46. Bian, D., Wu, Y., Song, G., Azizi, R. & Zamani, A. The application of mesenchymal stromal cells (MSCs) and their derivative exosome in skin wound healing: a comprehensive review. *Stem Cell Research & Therapy* **13**, 24 (2022).
47. Yang, Y. et al. Umbilical cord mesenchymal stem cell-derived exosomes promote wound healing and skin regeneration via the regulation of inflammation and angiogenesis. *Front Bioeng Biotechnol* **13**, 1641709 (2025).
48. Zhu, Z. et al. Exosomes derived from umbilical cord mesenchymal stem cells treat cutaneous nerve damage and promote wound healing. *Front Cell Neurosci* **16**, 913009 (2022).
49. Lo Sicco, C. et al. Mesenchymal stem cell-derived extracellular vesicles as mediators of anti-inflammatory effects: endorsement of macrophage polarization. *Stem Cells Transl Med* **6**, 1018-1028 (2017).

50. Xun, C., Deng, H., Zhao, J., Ge, L. & Hu, Z. Mesenchymal stromal cell extracellular vesicles for multiple sclerosis in preclinical rodent models: A meta-analysis. *Frontiers in Immunology* **Volume 13 - 2022**(2022).
51. Chinwalla, A.T. et al. Initial sequencing and comparative analysis of the mouse genome. *Nature* **420**, 520-562 (2002).
52. Howe, K.L. et al. Ensembl 2021. *Nucleic Acids Research* **49**, D884-D891 (2020).
53. Li, Q. et al. Extracellular vesicle-based mRNA therapeutics and vaccines. *Exploration (Beijing)* **5**, 20240109 (2025).
54. Li, J., Chen, S., Wang, H., Wang, W. & Liu, Y. Mesenchymal stem cells derived EXO-miR3671 delivery promoted angiogenesis and accelerated wound healing of diabetes. *Stem Cells* (2026).
55. El Andaloussi, S., Mäger, I., Breakefield, X.O. & Wood, M.J.A. Extracellular vesicles: biology and emerging therapeutic opportunities. *Nature Reviews Drug Discovery* **12**, 347-357 (2013).
56. Le, H.M. et al. Differential Development of Umbilical Cord-Derived Mesenchymal Stem Cells During Long-Term Maintenance in Fetal Bovine Serum-Supplemented Medium and Xeno- and Serum-Free Culture Medium. *Cellular Reprogramming* **23**, 359-369 (2021).
57. Vu, D.M. et al. Effects of Extracellular Vesicles Secreted by TGFβ-Stimulated Umbilical Cord Mesenchymal Stem Cells on Skin Fibroblasts by Promoting Fibroblast Migration and ECM Protein Production. *Biomedicines* **10**, 1810 (2022).
58. Dao, H.H. et al. Manufacturing exosomes for wound healing: Comparative analysis of culture media. *PLoS One* **19**, e0313697 (2024).
59. Nguyen, M.Q., Nguyen, D.D. & Than, U.T.T. The capacity of Wharton's jelly to prolong the survival of skin tissues ex vivo. *VNU Journal Of Science: Natural Sciences And Technology* **40**(2024).
60. Andrews, S. FastQC: A quality control tool for high throughput sequence data *Online at: https://www.bioinformatics.babraham.ac.uk/projects/fastqc/* (2010).
61. Martin, M. Cutadapt removes adapter sequences from high-throughput sequencing reads. *EMBnet.journal* **17**, 3 (2011).
62. Kim, D., Paggi, J.M., Park, C., Bennett, C. & Salzberg, S.L. Graph-based genome alignment and genotyping with HISAT2 and HISAT-genotype. *Nat Biotechnol* **37**, 907-915 (2019).
63. Zerbino, D.R. et al. Ensembl 2018. *Nucleic Acids Research* **46**, D754-D761 (2017).
64. Li, H. et al. The sequence alignment/Map format and SAMtools. *Bioinformatics* **25**, 2078-2079 (2009).
65. Liao, Y., Smyth, G.K. & Shi, W. FeatureCounts: an efficient general purpose program for assigning sequence reads to genomic features. *Bioinformatics* **30**, 923-930 (2013).
66. Ewels, P., Magnusson, M., Lundin, S. & Käller, M. MultiQC: summarize analysis results for multiple tools and samples in a single report. *Bioinformatics* **32**, 3047-3048 (2016).
67. Hita, A. et al. MGcount: a total RNA-seq quantification tool to address multi-mapping and multi-overlapping alignments ambiguity in non-coding transcripts. *BMC bioinformatics* **23**, 1-21 (2022).
68. Blighe, K., Rana, S. & Lewis, M. EnhancedVolcano: publication-ready volcano plots with enhanced colouring and labeling. *https://github.com/kevinblighe/EnhancedVolcano* (2021).
69. Warnes, G.R. et al. Gplots: various R programming tools for plotting Data. *https://cran.r-project.org/web/packages/gplots/index.html* (2025).
70. Yu, G., Wang, L.G., Han, Y. & He, Q.Y. Cluster Profiler: an R package for comparing biological themes among gene clusters. *Omics* **16**, 284-7 (2012).
71. Luo, W., Friedman, M.S., Shedden, K., Hankenson, K.D. & Woolf, P.J. GAGE: generally applicable gene set enrichment for pathway analysis. *BMC bioinformatics* **10**, 1-17 (2009).
72. Kanehisa, M. & Sato, Y. KEGG Mapper for inferring cellular functions from protein sequences. *Protein Sci* **29**, 28-35 (2020).

Author contributions

The conception and design of the study: UTTT, NHN, NTMH, and X-HN; Data collection: UTTT, HTTN, QMD, DMV, T-HN, NTMH, THN, X-HN, X-HD, HHD, HTP, QML; Analysis and interpretation of data: UTTT, HTTN, QMD, DMV, THN, NTMH, THN, X-HN, X-HD, HHD, HTP, QML; Manuscript drafting: UTTT, THN, QMD; Manuscript revising, UTTT, X-HN, NTMH, NHN; Final approval: NHN; Funding acquisition: NHN and UTTT.

Figures

Fig. 1

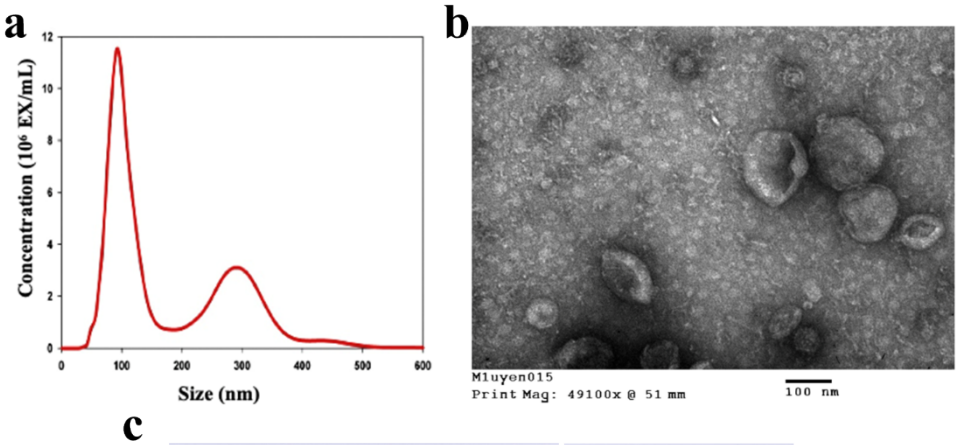

Characteristics of exosomes derived from UCMSCs. **a** Size distribution of exosomes that the majority of exosomes are around 100 nm. **b** Exosomes expressed a cup-shaped morphology and smooth surface; **c** Exosomal marker expression, that exosomes were detected with CD9, CD63, HSP70, and AGO2. Three separate exosome samples were analyzed: EX1, EX2, and EX3, respectively.

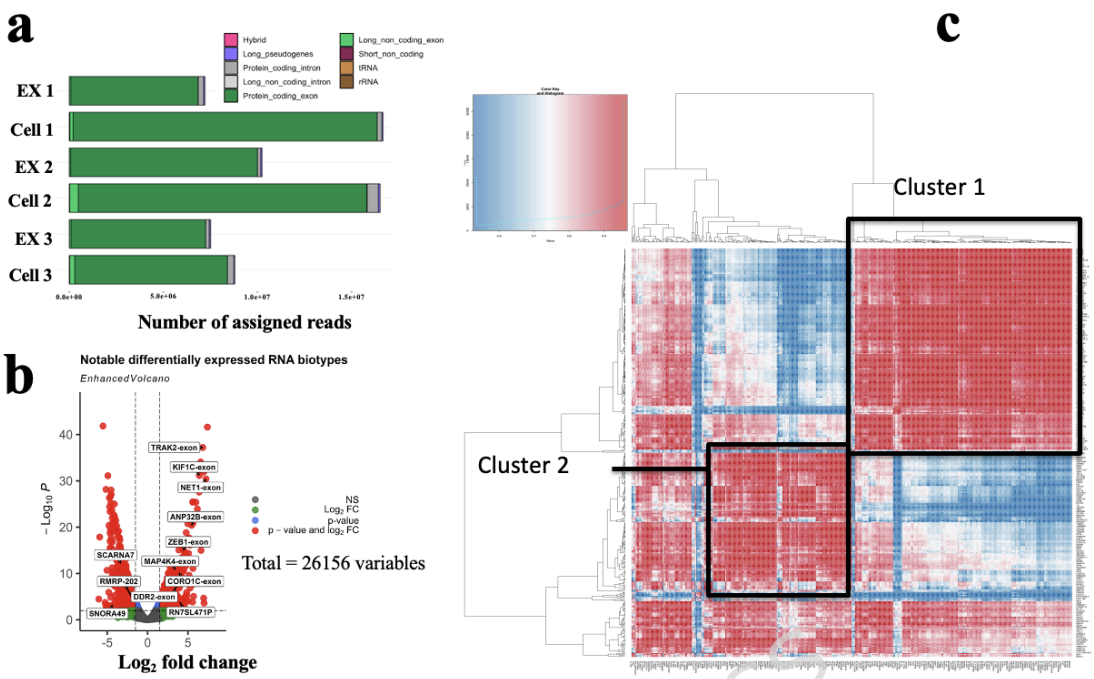

Fig. 2 mRNA biotype distribution and volcano plot indicated the notable genes detected in all samples. **a-b** The number of assigned reads belonging to each RNA subtype detected in UCMSC-derived exosomes. These include essential genes upregulated in UCMSC-derived exosomes associated with wound healing. Volcano plot shows the log2FC versus -log10(P-value) of all RNA biotypes. **c** Heatmap showcased top differential genes, a diagram depicting the overall approach.

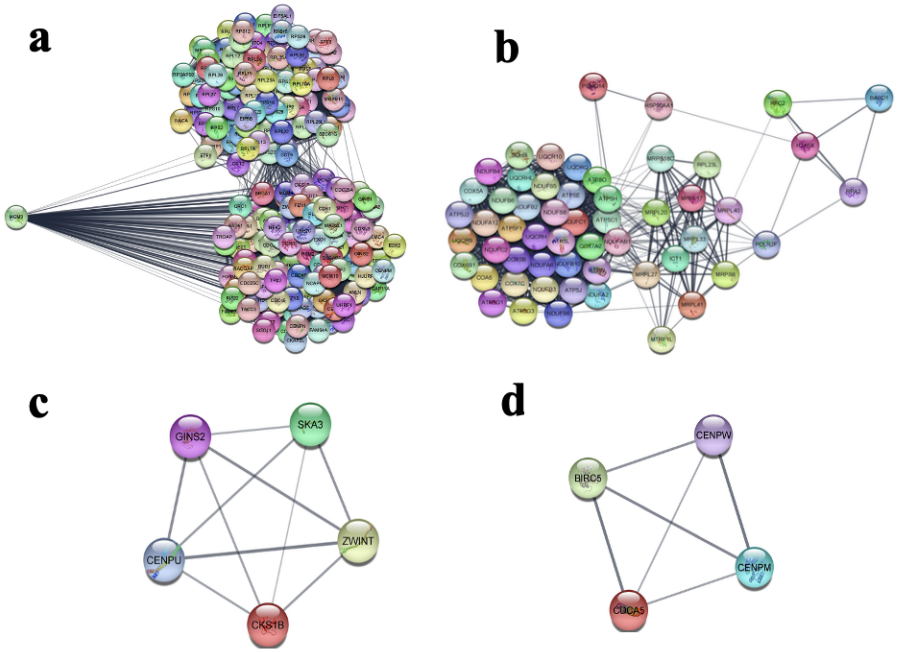

Fig. 3 String analysis showed the interaction network of proteins encoded by genes upregulated in exosomes. **a-b** Two major networks were generated by String, where the gene *MCM3* is a central hub within network A, and network B comprises connections to proteins associated with mitochondria and ATP synthase complex. **c-d** clusters of protein interactions deconvolved using MCODE from networks A and B.

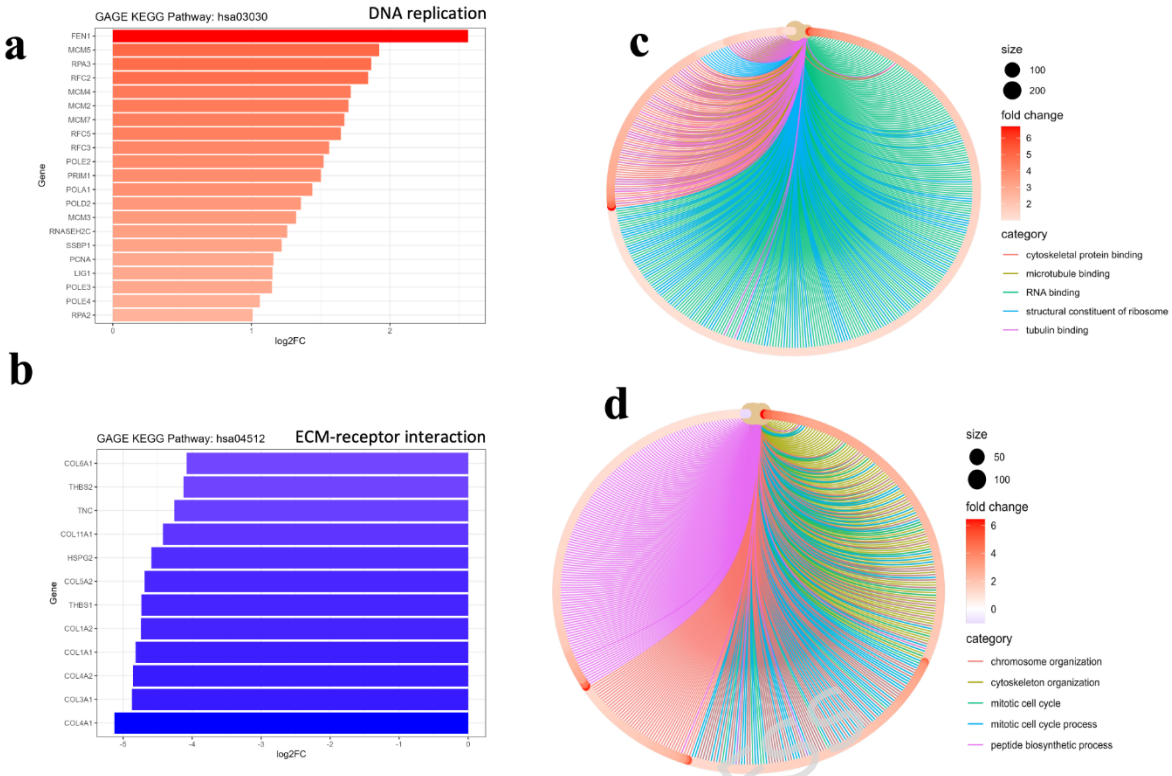

Fig. 4 KEGG pathway and GO term analysis genes detected in exosomes, with **a** the involvement of upregulated exosomal genes in DNA replication pathway; **b** the involvement of downregulated exosomal genes in ECM-receptor interaction pathway; **c** top five MF GO terms and **d** top five BP GO terms were revealed using the Cytoscape plug-in Molecular Complex Detection.

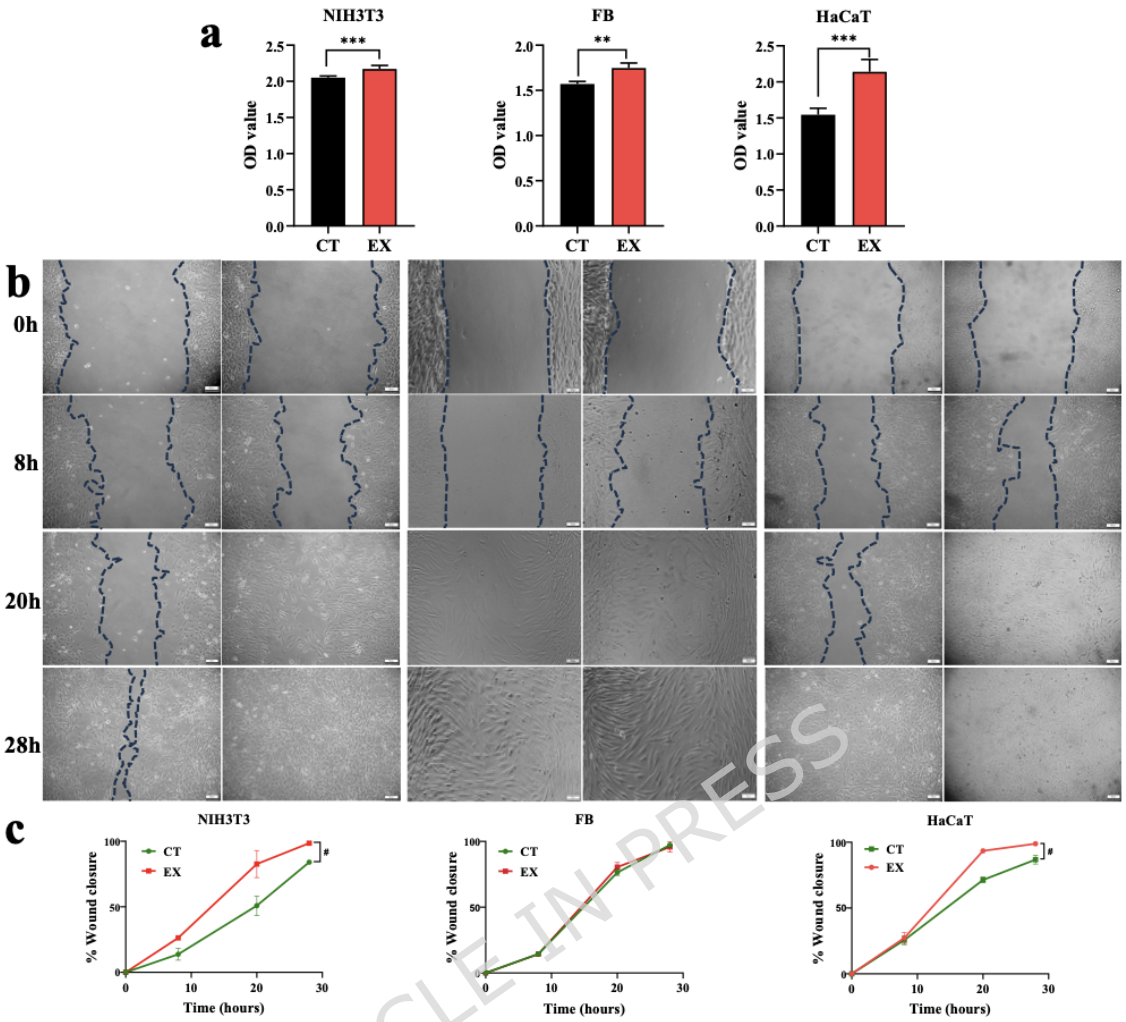

Fig. 5 Effect of EXs in wound healing *in vitro* (n = 3). **a** Capacity of EXs to stimulate dermal human fibroblast, NIH3T3, and HaCaT proliferation. **b** The image of cell migration followed the time of observation. **c** The quantification of wound closure rate (%). Scale bar: 50 μm.

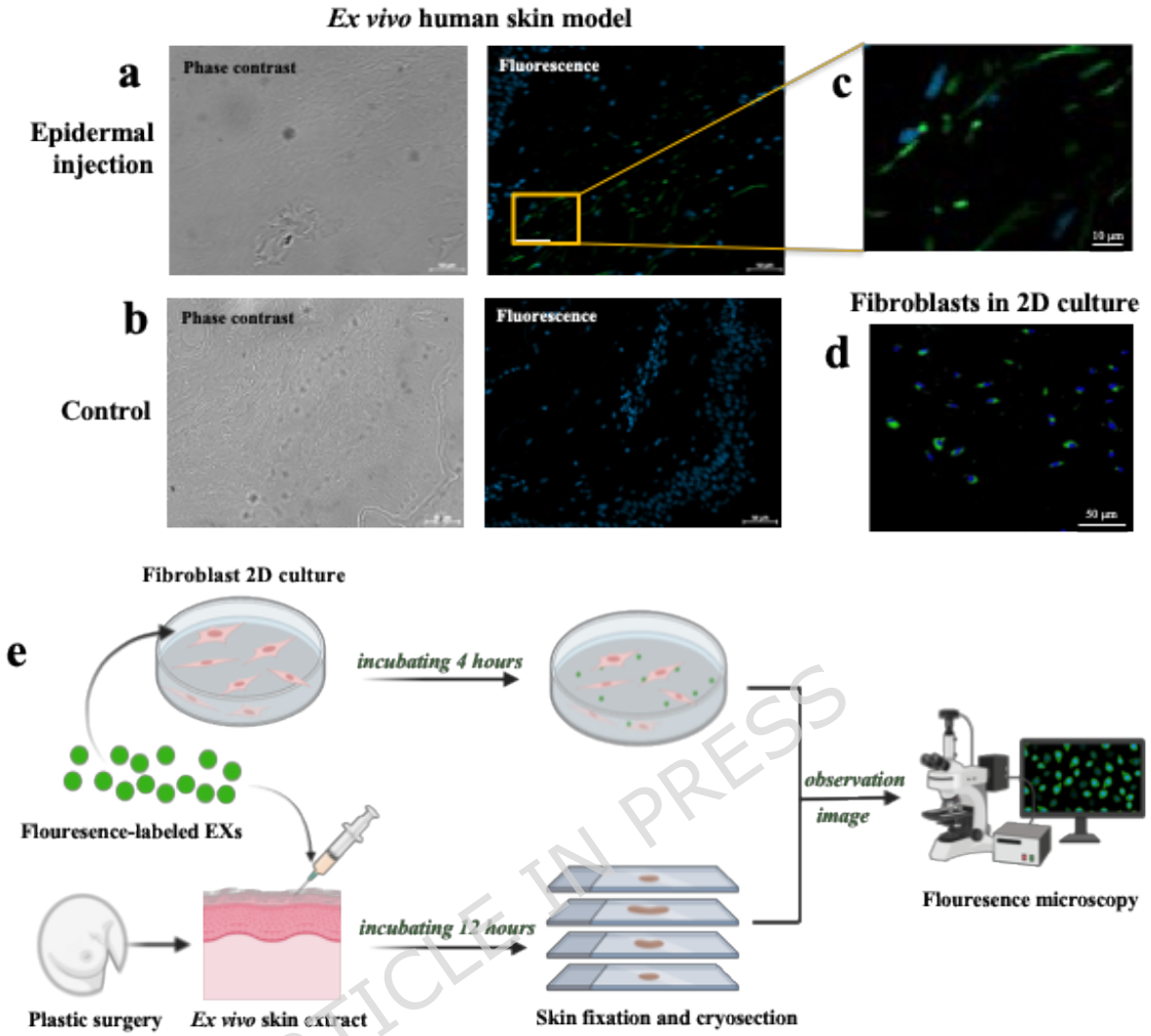

Fig. 6 The capacity of UCMSC-derived EXs penetrated into the dermis and were up-taken by cells (n = 3). **a, b,** & **c** The penetration of UCMSC-derived EXs into the dermis in the human skin model ex vivo after 12 hours. **d** UCMSC-derived EXs were up-taken by fibroblasts in 2D cell cultures after four hours. **e** The diagram shows the main steps in the experiments of UCMSC-EX penetration into the dermis and uptake by fibroblasts. Blue color (DAPI) indicates the nucleus, and green color indicates labeled-EVs (ExoGlow).

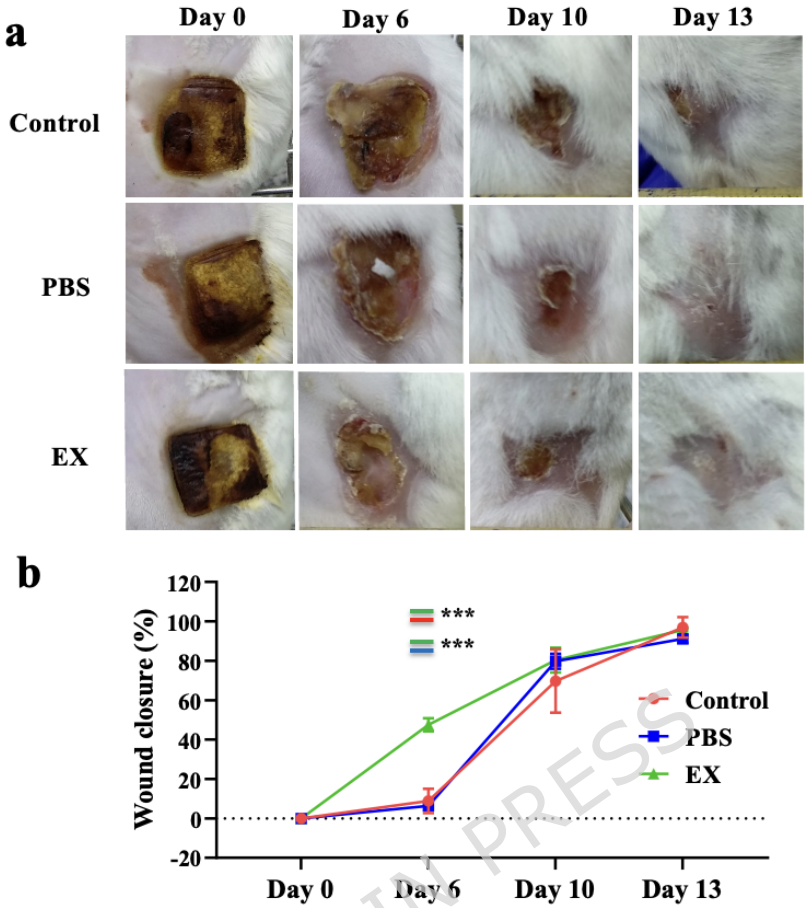

Fig. 7 Effect of EXs (from EX1 sample) in wound healing *in vivo*. **a** Images of the burned site on mice in different groups: control, PBS, and EX treatment. **b** Burned animal models indicate that EXs have effects on stimulating the wound closing faster in the early days after wounded skin. This efficacy decreased from day ten onward. Control: no treatment; PBS: burned animal models treated with PBS; EX: burned animal models treated with exosomes. Results were averages of 3 biological samples (n = 3). Statistical significance was determined by Two-Way ANOVA and indicated by *** where $p < 0.001$. Error bars indicate ± SD.